

# Theory of Hole-Spin Qubits in Strained Germanium Quantum Dots

L. A. Terrazos,<sup>1</sup> E. Marcellina,<sup>2</sup> S. N. Coppersmith,<sup>3, 2</sup> Mark Friesen,<sup>3</sup> A. R. Hamilton,<sup>2</sup> Xuedong Hu,<sup>4</sup> Belita Koiller,<sup>5</sup> A. L. Saraiva,<sup>5</sup> Dimitrie Culcer,<sup>2</sup> and Rodrigo B. Capaz<sup>5</sup>

<sup>1</sup>*Centro de Educação e Saúde, Universidade Federal de Campina Grande, Cuité, PB 58175-000, Brazil*

<sup>2</sup>*School of Physics, University of New South Wales, Sydney 2052, Australia*

<sup>3</sup>*Department of Physics, University of Wisconsin-Madison, Madison, Wisconsin 53706, USA*

<sup>4</sup>*Department of Physics, University at Buffalo, SUNY, Buffalo, New York 14260-1500, USA*

<sup>5</sup>*Instituto de Física, Universidade Federal do Rio de Janeiro, CP 68528, 21941-972 RJ, Brazil*

(Dated: June 18, 2022)

We theoretically investigate the properties of holes in a  $\text{Si}_x\text{Ge}_{1-x}/\text{Ge}/\text{Si}_x\text{Ge}_{1-x}$  quantum well in a perpendicular magnetic field that make them advantageous as qubits, including a large ( $>100$  meV) intrinsic splitting between the light and heavy hole bands, a very light ( $\sim 0.05 m_0$ ) in-plane effective mass, consistent with higher mobilities and tunnel rates, and larger dot sizes that could ameliorate constraints on device fabrication. Compared to electrons in quantum dots, hole qubits do not suffer from the presence of nearby quantum levels (e.g., valley states) that can compete with spins as qubits. The strong spin-orbit coupling in Ge quantum wells may be harnessed to implement electric-dipole spin resonance, leading to gate times of several nanoseconds for single-qubit rotations. The microscopic mechanism of this spin-orbit coupling is discussed, along with its implications for quantum gates based on electric-dipole spin resonance, stressing the importance of coupling terms that arise from the underlying cubic crystal field. Our results provide a theoretical foundation for recent experimental advances in Ge hole-spin qubits.

## I. INTRODUCTION

Hole spin qubits in strained germanium possess favorable properties for quantum computing, including (1) the absence of valley degeneracy, which would otherwise compete with the spin degree of freedom for qubits formed in the conduction band of Si or Ge [1], (2) the high natural abundance of spin-0 nuclear isotopes in Ge, which may be further purified, (3) the formation of hole states in *p*-type atomic orbitals whose wavefunction nodes occur at nuclear sites, suppressing unwanted hyperfine interactions [2, 3], and (4) the very light in-plane effective mass [4–7], allowing for larger dots and relaxing constraints on device fabrication. The light mass also improves carrier mobilities, which can exceed  $10^6 \text{ cm}^2/\text{Vs}$  for 2D Ge hole gases [4]. Leveraging these strengths, rapid progress has been made in implementing high-fidelity one and two-qubit gate operations [5, 8–16].

Several of the most important advantages for qubits, such as the lifting of level degeneracy at the valence-band edge, the light effective mass, and access to Rashba spin-orbit coupling (SOC), which enables fast gate operations, are not available in the bulk. Rather, they emerge in SiGe/Ge/SiGe quantum wells due to confinement or strain. In fact, some properties (e.g., the light mass) are completely unexpected from the bulk band structure.

In this work, we provide a theoretical foundation for the emergent physics of Ge quantum wells, and explanations for recent experimental observations, through detailed *ab initio* band-structure calculations. We gain further insight into the origins of qubit-friendly materials properties by performing  $\mathbf{k}\cdot\mathbf{p}$  calculations. We place special emphasis on understanding the Rashba coupling, and the unexpected matrix element that connects states with orbital quantum numbers that differ by one. Taken to-

gether, these ingredients enable electrically driven spin flips via electric-dipole spin resonance (EDSR), with fast, single-qubit gate times of order 0.2 GHz. In contrast with other recent work [15], we propose here to exploit the large out-of-plane value of the Landé *g*-factor, so that relatively small external magnetic fields are needed for gate operation, making the qubit more compatible with superconducting gate structures, such as microwave resonators. A large *g*-factor also helps to define the qubit with respect to thermal broadening.

The paper is organized as follows. In Sec. II, we provide technical details of the theoretical methods used in this work. We describe the model system, including the heterostructure and top gates (Fig. 1). We summarize the *ab initio* simulations of the quantum-well portion of the device and our  $\mathbf{k}\cdot\mathbf{p}$  Hamiltonian. We describe our theoretical approach for modeling EDSR in two steps. We first outline a model for electron confinement in the vertical direction (perpendicular to the plane of the quantum well) and the lateral confinement of a quantum dot, and use this to obtain the effective Rashba spin-orbit Hamiltonian for our geometry. We then use this to determine the EDSR Rabi frequency when applying an in-plane ac electric field. In Sec. III, we describe the main results of our calculations, including the band-structure details obtained by *ab initio* methods (Fig. 2), the corresponding in-plane and out-of-plane effective masses as a function of Ge concentration and strain (Fig. 3), and the energy splittings between the valence bands (Fig. 4). We then apply  $\mathbf{k}\cdot\mathbf{p}$  methods to help clarify the origins of energy-level splitting, and the lifting of degeneracy, by artificially separating the effects of strain and SOC (Fig. 5). Finally, we use our EDSR analysis to estimate the expected Rabi frequency for a realistic range of device parameters (Figs. 6 and 7). In Sec. IV, we discuss

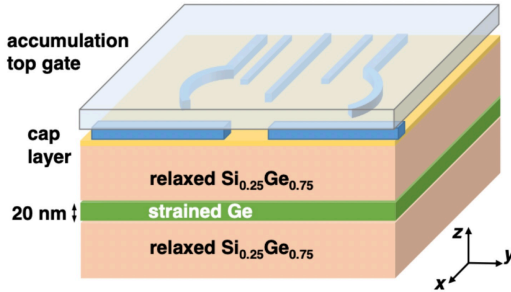


FIG. 1. Cartoon depiction of a typical heterostructure and gate stack of a strained-Ge quantum well used to form hole-spin qubits in quantum dots. Here, a 20 nm strained-Ge quantum well is grown epitaxially on a strain-relaxed  $\text{Si}_{0.25}\text{Ge}_{0.75}$  alloy. For this arrangement, the strain in the Ge layer is  $\varepsilon \approx -1\%$ , as consistent with Eq. (1). In addition to metal depletion gates (blue) and interspersed oxide layers (yellow), we assume a global top gate (transparent gray) that can accumulate a 2D hole gas in the quantum well in the absence of doping. Here,  $z$  is defined as the growth direction.

our results and conclude by reviewing the predominant decoherence mechanisms for Ge hole qubits.

## II. METHODS

We consider a typical, electrically gated double-dot device such as the one schematically depicted in Fig. 1. The essential features include a SiGe/Ge/SiGe heterostructure, an optional capping layer, and a set of patterned, nanometer-scale metal gates that are isolated from the heterostructure by oxide layer(s). When sandwiched between strain-relaxed, Ge-rich SiGe alloys, the compressively strained Ge forms a type-I quantum well that can trap either electrons or holes [17], although we focus exclusively on holes here. Note that the details of the gate and oxide layers are unimportant for the following discussion.

For the heterostructure, we specifically consider an accumulation-mode gating scheme [18–20] with no dopants. The SiGe barriers should be high enough to form a quantum well. For example, a strain-relaxed  $\text{Si}_{0.25}\text{Ge}_{0.75}$  barrier gives a valence-band offset of  $\sim 170$  meV [17], which is ample for trapping holes. The heterostructure growth typically begins on a Si wafer. [Here, we assume a Si (001) substrate.] Due to lattice mismatch, the growth of SiGe alloy on Si induces dislocations that are harmful for device operation. Such effects can be mitigated by increasing the Ge content gradually, over several  $\mu\text{m}$ , until the desired alloy is achieved; under ideal conditions, the resulting SiGe growth surface is strain-relaxed and dislocation-free [21]. Alternative approaches, such as reverse grading, are also common [4, 5]. A pure Ge quantum well is then grown on the SiGe virtual substrate. The width of the well should be less than the critical thickness for forming additional dislocations;

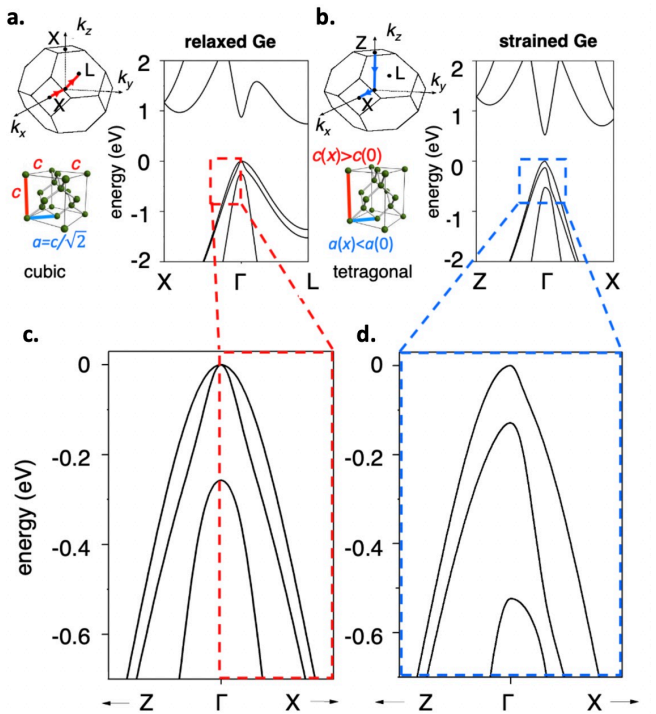


FIG. 2. Electronic band structures for (a) relaxed vs. (b) uniaxially-strained Ge, obtained using DFT. To the left of each plot we show the corresponding real and reciprocal space crystal structures (lower and upper diagrams, respectively), with lattice constants ( $a$  and  $c$ ) and symmetry points ( $\Gamma$ ,  $X$ ,  $Z$ , and  $L$ ), as indicated. [Note that the tetragonal deformation is exaggerated in (c), for clarity.] (c),(d) Blown-up band structures corresponding to (a) and (b). Here, we focus on the [100] ( $x$ ) and [001] ( $z$ ) axes because of their relevance for quantum dot formation, and we note that [100] and [010] are equivalent. In (a) and (c), cubic symmetry also makes the  $X$  and  $Z$  points equivalent and enforces a degeneracy between the top two hole bands at the  $\Gamma$  point. The lowest or “split-off” band is completely detached from the others. Away from the singular  $\Gamma$  point, the hole bands are all doubly-degenerate. In (b) and (d), the  $x$ - $z$  degeneracy is lifted and only the  $x$ - $y$  degeneracy remains. The resulting band structure is highly anisotropic.

however, this is not typically a problem for Ge-rich alloys. For example, the critical Ge thickness of a  $\text{Si}_{0.25}\text{Ge}_{0.75}$  barrier is  $\sim 30$  nm [22]. Finally, we note that Ge forms unstable oxides [23] (similar problems also occur for SiGe alloys [24]); it may therefore be beneficial to include a silicon capping layer, with a carefully chosen thickness [25].

### A. Density Functional Theory

Realistic, quantitative predictions for the band structure of strained Ge are key for assessing the viability of hole-spin qubits. In this work, we compute the band structure using self-consistent, *ab initio* density functional theory (DFT), including spin-orbit interactions.

The calculations are performed using the full-potential linearized augmented plane wave method (FP-LAPW), as implemented in the Wien2k package [26]. Using the augmented plane wave plus local orbital (APW+lo) basis set [27–29], the wavefunctions are expanded in spherical harmonics inside non-overlapping atomic spheres, with “muffin-tin” radii  $R_{\text{MT}}$ , and in plane waves for the rest of the unit cell (the interstitial region). In the present calculations we adopt  $R_{\text{MT}}=0.95$  Å for Ge, and use 405  $\mathbf{k}$  points in the irreducible wedge of the Brillouin zone. For the spherical-harmonic expansion, the maximum orbital angular momentum is taken to be  $l_{\text{max}}=10$ , while the plane-wave expansion in the interstitial region is extended to  $k_{\text{max}}=9.0/R_{\text{MT}}=9.47$  Å<sup>-1</sup>, and the charge density is Fourier expanded up to  $G_{\text{max}}=12$  Ry. (These simulation parameters were all checked and found to yield numerical convergence.) Electron-electron interactions are described using the modified Becke-Johnson exchange potential + local density approximation (LDA) correlations [30, 31], which is known to yield accurate calculations of band gaps in semiconductors.

The primitive Bravais lattice used in our simulations is body-centered tetragonal with a two-atom basis consistent with the diamond structure. Details of the real and reciprocal lattice structure are depicted in the insets of Figs. 2(a) and 2(b). For unstrained Ge, the tetragonal lattice parameters are given by  $a=b=4.0008$  Å in the plane of the quantum well, and  $c=\sqrt{2}a=5.6580$  Å in the growth direction. For a  $\text{Si}_x\text{Ge}_{1-x}$  alloy with concentration  $x$ , the lattice constant  $a(x)$  is modified, and if the quantum well is grown pseudomorphically, the same lat-

tice constant is also imposed on the strained Ge. We define the compressive strain as

$$\varepsilon(x) = [a(x) - a(0)]/a(0) < 0. \quad (1)$$

For the SiGe alloy, Vegard’s law gives  $\varepsilon(x) = -0.04x$ , while Poisson’s ratio for germanium gives  $\nu = 0.27 = -[c(x) - c(0)]/[a(x) - a(0)]$  [32]. Combining these formulas yields an analytical expression for  $c(x)$ .

The main results of our DFT calculations are reported in Sec. III A. To simplify the calculations, we do not specifically consider a quantum well geometry. Instead, we adopt a range of strain parameters consistent with a strained Ge quantum well sandwiched between strain-relaxed  $\text{Si}_x\text{Ge}_{1-x}$  for the range  $x \in (0, 0.25)$ . From the previous discussion, this corresponds to compressive strains in the range  $\varepsilon \in (-1, 0)$  percent.

## B. $\mathbf{k}\cdot\mathbf{p}$ Theory for Strained Germanium

$\mathbf{k}\cdot\mathbf{p}$  theory provides insight into energy-splitting mechanisms associated with SOC and strain for the top-most valence bands. We consider the  $6 \times 6$  Luttinger-Kohn-Pikus-Bir (LKPB) Hamiltonian, which incorporates strain through the Bir-Pikus model [33]. The deformation potentials are obtained using a linear approximation for the dependence of the energy bands on strain [34]. In the basis of total angular momentum eigenstates,  $|j, m_j\rangle \in \{|\frac{3}{2}, \frac{3}{2}\rangle, |\frac{3}{2}, \frac{1}{2}\rangle, |\frac{3}{2}, -\frac{1}{2}\rangle, |\frac{3}{2}, -\frac{3}{2}\rangle, |\frac{1}{2}, \frac{1}{2}\rangle, |\frac{1}{2}, -\frac{1}{2}\rangle\}$ , the LKPB Hamiltonian is given by

$$H_{\text{LKPB}} = \begin{pmatrix} P+Q & -S & R & 0 & -S/\sqrt{2} & \sqrt{2}R \\ -S^* & P-Q & 0 & R & -\sqrt{2}Q & \sqrt{3/2}S \\ R^* & 0 & P-Q & S & \sqrt{3/2}S^* & \sqrt{2}Q \\ 0 & R^* & S^* & P+Q & -\sqrt{2}R^* & -S^*/\sqrt{2} \\ -S^*/\sqrt{2} & -\sqrt{2}Q^* & \sqrt{3/2}S & -\sqrt{2}R & P+\Delta & 0 \\ \sqrt{2}R^* & \sqrt{3/2}S^* & \sqrt{2}Q^* & -S/\sqrt{2} & 0 & P+\Delta \end{pmatrix}, \quad (2)$$

where

$$\begin{aligned} P &= P_k + P_\varepsilon, & Q &= Q_k + Q_\varepsilon, \\ R &= R_k + R_\varepsilon, & S &= S_k + S_\varepsilon. \end{aligned} \quad (3)$$

Here, the  $k$  subscripts denote the Luttinger-Kohn Hamiltonian matrix elements, defined as [35]

$$\begin{aligned} P_k &= \frac{\hbar^2}{2m_0} \gamma_1 (k_x^2 + k_y^2 + k_z^2), & Q_k &= -\frac{\hbar^2}{2m_0} \gamma_2 (2k_z^2 - k_x^2 - k_y^2), \\ R_k &= \sqrt{3} \frac{\hbar^2}{2m_0} [-\gamma_2 (k_x^2 - k_y^2) + 2i\gamma_3 k_x k_y], & S_k &= \sqrt{3} \frac{\hbar^2}{m_0} \gamma_3 (k_x - ik_y) k_z, \end{aligned} \quad (4)$$

while the  $\varepsilon$  subscripts denote the Bir-Pikus strain matrix elements, defined as [33]

$$\begin{aligned} P_\varepsilon &= -a_v (\varepsilon_{xx} + \varepsilon_{yy} + \varepsilon_{zz}), & Q_\varepsilon &= -\frac{b_v}{2} (\varepsilon_{xx} + \varepsilon_{yy} - 2\varepsilon_{zz}), \\ R_\varepsilon &= \frac{\sqrt{3}}{2} b_v (\varepsilon_{xx} - \varepsilon_{yy}) - id\varepsilon_{xy}, & S_\varepsilon &= -d_v (\varepsilon_{xz} - i\varepsilon_{yz}), \end{aligned} \quad (5)$$

where  $m_0$  is the bare electron mass,  $\gamma_1=13.38$ ,  $\gamma_2=4.24$ ,

and  $\gamma_3=5.69$  are Luttinger parameters [35],  $a_v=2.0$  eV,

$b_v = -2.16$  eV, are  $d_v = -6.06$  eV are deformation potential parameters [36], and  $\{\varepsilon_{ij}\}$  are strain tensor components. Experiments in bulk, relaxed Ge [17] give  $\Delta = 0.296$  eV as the energy splitting of the split-off band below the light and heavy-hole bands at  $\mathbf{k} = 0$ ; this value is taken as an input parameter in the present work. Note that  $\varepsilon_{xx} (= \varepsilon_{yy})$  is equivalent to  $\varepsilon(x)$ , defined in Sec. II A. The Pikus-Bir expressions in Eq. (5), are generic. In this work, we focus on the special case of uniaxial strain, for which  $\varepsilon_{zz} = -2(C_{12}/C_{11})\varepsilon_{xx}$  and  $\varepsilon_{xy} = \varepsilon_{yz} = \varepsilon_{zx} = 0$ , leading to  $R_\varepsilon = S_\varepsilon = 0$ , and we adopt  $C_{11} = 129.2$  GPa and  $C_{12} = 47.9$  GPa as the elastic stiffness constants for the strain-stress tensor [32]. The resulting strain splits the fourfold-degenerate valence band edge into two twofold-degenerate levels. The main results of these calculations are presented in Sec. III B.

### C. Calculating the Rashba Spin-Orbit Coupling

There are two prerequisites for observing Rashba SOC in a quantum well: a broken structural symmetry and an intrinsic SOC. The broken symmetry is provided here by an asymmetric confinement potential of the form

$$V_z(z) = \begin{cases} eF_z z & (|z| < d/2) \\ \infty & (\text{otherwise}) \end{cases}, \quad (6)$$

where  $F_z$  is the average electric field across the quantum well, and the well width,  $d = 20$  nm, is held fixed for all our calculations. (Note that  $d$  is not an important parameter in this calculation, since the electric field draws the hole wavefunction to the top of the quantum well, so that it does not interact strongly with the bottom of the well.) The total Hamiltonian for the vertical confinement of holes is then given by

$$H_z = H_{\text{LKPB}}(k^2, \hat{k}_z) + V_z(z), \quad (7)$$

where  $\hat{k}_z \equiv -i\frac{\partial}{\partial z}$ .

To evaluate Eq. (7), we first truncate  $H_{\text{LKPB}}$  to the four-dimensional,  $j = 3/2$  subspace and introduce variational, effective-mass wavefunctions for the two bands corresponding to  $|m_j| \in \{1/2, 3/2\}$  [37]:

$$\varphi_i(z) = \begin{cases} \frac{\sin\left[\frac{\pi}{d}(z + \frac{d}{2})\right] \exp[-b_i(\frac{z}{d} + \frac{1}{2})]}{\pi \sqrt{d \frac{\exp(-b_i) \sinh(b_i)}{2\pi^2 b_i + 2b_i^3}}} & (|z| < d/2) \\ 0 & (\text{otherwise}) \end{cases}. \quad (8)$$

Here,  $i$  is the band index and  $\{b_i\}$  are the corresponding variational parameters. We determine  $b_i$  by minimizing the eigenvalues of  $H_z$  in the limit of  $k = 0$ , in which case the Hamiltonian is already diagonal and the bands decouple.

A large intrinsic SOC occurs naturally for holes in Ge due to the coupling between the different valence bands. We compute the effective Hamiltonian for holes in the topmost ( $|m_j| = 3/2$ ) band by applying a Schrieffer-Wolff transformation to Eq. (7), using the states shown in

Eq. (8), to eliminate the coupling to the second band [38], obtaining  $H_0 + H_R$ , where  $H_0 = \hbar^2(k_x^2 + k_y^2)/2m_x$  is the kinetic energy in the effective mass approximation. The effective Rashba Hamiltonian can be expressed as the sum of two terms,

$$H_R = i\alpha_{R2}(k_+^3\sigma_- - k_-^3\sigma_+) + i\alpha_{R3}(k_+k_-k_+\sigma_+ - k_-k_+k_-\sigma_-), \quad (9)$$

where  $\sigma_\pm = \sigma_x \pm i\sigma_y$  are Pauli spin matrices, and the coupling constants  $\alpha_{R2}$  and  $\alpha_{R3}$  are derived in Ref. [38]. Here,  $\alpha_{R2}$  arises from the spherically symmetric component of the Luttinger-Kohn Hamiltonian, while  $\alpha_{R3}$  arises from the cubic-symmetric component.

### D. Calculating the ESDR Rabi Frequency

There are also several prerequisites for implementing EDSR: an artificial [39] or intrinsic SOC, a large, static magnetic field to define the quantization axis, and an in-plane ac electric field. Here, we assume Rashba SOC, as described in the previous section. Contrary to other proposals that we have seen, we also assume an out-of-plane  $B$ -field whose orientation takes advantage of the large out-of-plane  $g$ -factor [40],  $g_z$ , to reduce the constraints on the field magnitude. The effective qubit Hamiltonian for EDSR is then given by

$$H_q = H_0(\mathbf{k} \rightarrow -i\nabla - e\mathbf{A}/\hbar) + H_R(\mathbf{k} \rightarrow -i\nabla - e\mathbf{A}/\hbar) + V_d(x, y) + (g_z/2)\mu_B B_z \sigma_z + eE_{\text{ac}} x \cos(\omega t) \sigma_x, \quad (10)$$

where  $\mathbf{A} = (B_z/2)(-y, x, 0)$ . For a circular, parabolic dot, we assume an electrostatically defined confinement potential of the form

$$V_d(x, y) = \frac{1}{2}m_x\omega_0^2(x^2 + y^2), \quad (11)$$

where  $\hbar\omega_0$  is the energy splitting between the orbital levels when  $B_z = 0$ . If we now assume that  $B_z > 0$ , but set  $E_{\text{ac}} = 0$ , the eigenstates of  $H_q$  are defined as Fock-Darwin orbitals [41, 42], for which the ground state ( $n = 0$ ) is given by

$$\phi_0(x, y) = \frac{1}{a_0\sqrt{\pi}} \exp\left[-(x^2 + y^2)/2a_0^2\right], \quad (12)$$

and the first excited states ( $n = 1$ ) are given by

$$\phi_{\pm 1}(x, y) = \frac{2}{a_0^2\sqrt{\pi}}(x \pm iy) \exp\left[-(x^2 + y^2)/2a_0^2\right]. \quad (13)$$

For an out-of-plane magnetic field, we note that the dot is confined both electrostatically and magnetically, with an effective radius of  $a_0 = \sqrt{\hbar/|eB|}/(1/4 + \omega_0^2/\omega_c^2)^{1/4}$ , where  $\omega_c = |eB|/m_x$  is the cyclotron frequency.

For hole-spin qubits, the logical (spin) states are formed exclusively within the ground-state orbital,  $\phi_0$ .

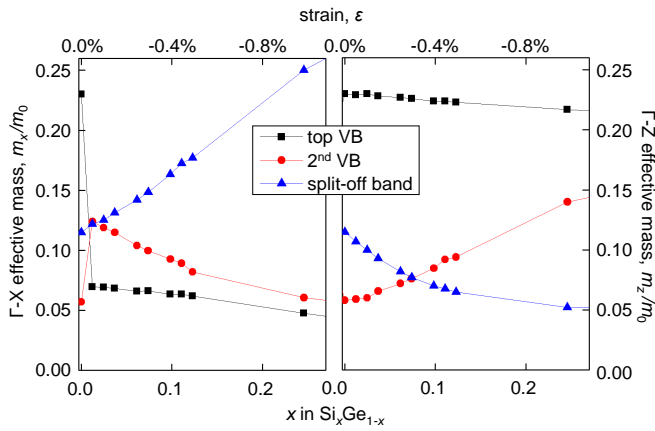


FIG. 3. Effective masses for the top three valence bands, in units of the free-electron rest mass  $m_0$ , obtained using DFT. Due to uniaxial strain along [001], the masses in different directions,  $m_x^*$  and  $m_z^*$ , are inequivalent. While  $m_z^*$  is found to vary smoothly with substrate composition,  $m_x^*$  changes abruptly near  $x \approx 0$ , indicating an inversion of the band character: the top band becomes lighter than the second band, as consistent with the right-hand side of Fig. 2(d).

However, the EDSR spin-flip mechanism involves virtual transitions to  $\phi_{\pm 1}$  via a second-order process that combines ac driving and SOC. The driving term in Eq. (10),  $eE_{ac}x \cos(\omega t)$ , is applied through one of the nearby top gates [43], generating an orbital transition with  $\Delta n = \pm 1$ . Initial proposals for hole-based EDSR [2] therefore required Dresselhaus SOC, which can generate such  $\Delta n = \pm 1$  transitions. For group-IV materials, however, the Dresselhaus mechanism is normally absent. Moreover, the dominant  $\alpha_{R2}$  term of the Rashba coupling, Eq. (9), is cubic in  $k$ , as consistent with  $\Delta n = \pm 3$ , and therefore does not support EDSR. An important conclusion of the present work is that the  $\alpha_{R3}$  term, which is not typically considered in such calculations, provides the required  $\Delta n = \pm 1$  transitions that support EDSR. In what follows, we focus exclusively on this term.

To calculate the EDSR Rabi frequency  $f_R$ , we evaluate the full Hamiltonian, Eq. (10), using the Fock-Darwin basis states, and perform a Schrieffer-Wolff transformation to eliminate the coupling to the excited states. For resonant driving, with  $\omega = \sqrt{\omega_0^2 + \omega_c^2}/4$ , we obtain

$$hf_R = -\frac{eE_{ac}\alpha_{R3}}{2a_0^2} \left[ \left( \frac{1}{\Delta_1} + \frac{1}{\Delta_2} \right) - \left( \frac{1}{\Delta_3} + \frac{1}{\Delta_4} \right) \right] - \frac{e^2 E_{ac} \alpha_{R3} B_z}{4\hbar} \left[ \left( \frac{1}{\Delta_1} + \frac{1}{\Delta_2} \right) + \left( \frac{1}{\Delta_3} + \frac{1}{\Delta_4} \right) \right], \quad (14)$$

where

$$\begin{aligned} \Delta_1 &\equiv -\hbar\omega - \frac{1}{2}\hbar\omega_c, \\ \Delta_2 &\equiv -\hbar\omega - \frac{1}{2}\hbar\omega_c - g\mu_B B_z, \\ \Delta_3 &\equiv -\hbar\omega + \frac{1}{2}\hbar\omega_c + g\mu_B B_z, \\ \Delta_4 &\equiv -\hbar\omega + \frac{1}{2}\hbar\omega_c. \end{aligned} \quad (15)$$

This result is explicitly proportional to  $E_{ac}\alpha_{R3}$ . Moreover,  $f_R$  is found to be linear in  $B_z$ , as readily verified

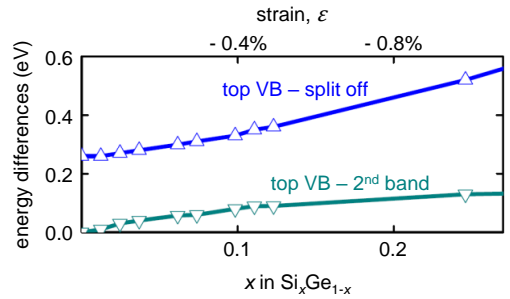


FIG. 4. Energy differences between the hole bands at the  $\Gamma$  point as a function of the Si concentration in the substrate,  $x$ , obtained using DFT. Upward-pointing blue triangles correspond to the splitting between the top of the valence band and the split-off band, while downward-pointing teal triangles show the splitting between the first and second bands.

by expanding Eq. (14) in powers of (small)  $B_z$ . Based on these results, and those of the previous section, we estimate the Rabi frequencies that could be expected in realistic quantum dot devices, as described in Sec. III D.

### III. RESULTS

In this section we present the main results of each of the previous calculations.

#### A. DFT Estimates

DFT results are plotted in the main panels of Figs. 2(a) and 2(b), where we compare Ge band structures for the cases of  $x = 0$  (unstrained Ge) and  $x = 0.25$  (strained Ge). In the first case, the cubic symmetry ensures that the energy dispersion is identical for wavevectors in the plane of the quantum well ( $k_x, k_y$ ) and the growth direction ( $k_z$ ). (Here, the subscript  $x$  refers to the [100] axis, not the alloy composition.) In the second case, the X and Z points are inequivalent; both are shown in the figure. Focusing on holes, Figs. 2(c) and 2(d) show blown-up views of the top of the valence band. Since the quantum dot wave functions are constructed mainly from Bloch states at the very top of the band, the essential physics is captured in the band curvature at the  $\Gamma$  point, which is proportional to the inverse effective mass. In the case of strain, we observe anisotropic behavior in the  $x$  (in-plane) and  $z$  (out-of-plane) directions. Figures 2(c) and 2(d) also highlight the large energy splitting between light and heavy hole bands under strain, which is crucial for defining the qubit states.

Figure 3 provides a more detailed picture of the in-plane ( $m_x^*$ ) and out-of-plane ( $m_z^*$ ) effective masses, obtained for strains in the range  $\epsilon \in (-1, 0)$  percent. The corresponding values of  $x$  in the  $\text{Si}_x\text{Ge}_{1-x}$  barrier alloy are also shown. We note that the in-plane mass of the top two bands changes abruptly near  $x=0$ . Remarkably,  $m_x^*$

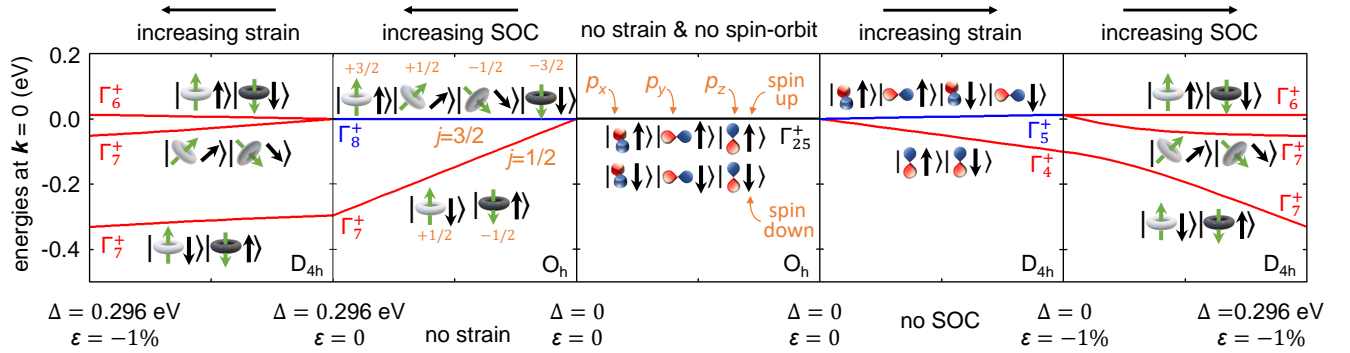


FIG. 5. Energy levels calculated at the  $\Gamma$  point, using the  $\mathbf{k}\cdot\mathbf{p}$  method, at zero magnetic field, which allows us to artificially decouple the effects of SOC (represented by the split-off band gap  $\Delta$  of bulk Ge) and strain ( $\varepsilon$ ). The five panels show results when these two parameters are independently varied between zero and their final values, corresponding to a strained quantum well with  $x=0.25$ . Level degeneracies are indicated by color: black for sixfold, blue for fourfold, and red for twofold. The point symmetry groups and corresponding irreducible representations for the hole states are indicated in each case. The center panel represents the case with no SOC and no strain, in which the  $p_x$ ,  $p_y$ , and  $p_z$  orbitals and both spin states are degenerate. Moving to the right, the strain is increased without including SOC, yielding a fourfold degenerate band spanned by  $p_x$  and  $p_y$ , and a twofold degenerate  $p_z$  band. Including SOC, the  $p$  orbitals hybridize, creating states with different combinations of orbitals (represented now as tori) and spins, resulting in three doublets. Moving from the center panel to the left, including SOC but no strain yields a split-off, doubly-degenerate  $j=1/2$  band and a fourfold degenerate  $j=3/2$  band, as consistent with bulk, relaxed Ge at the  $\Gamma$  point. We represent these states in a classical picture as having orbital angular momenta and spins either parallel (upper quadruplet) or anti-parallel (lower doublet). The different values of orbital angular momenta are represented by the colors of the orbital (darker tones for lower  $m_j$ ) and by the inclination of the green vectors in relation to the vertical direction. Including strain, the bands hybridize slightly such that  $j$  is no longer a good quantum number. Here, the fully strained spectrum is identical to the far right-hand side of the figure.

becomes lightest for the top band, over the experimental regime of interest ( $x \gtrsim 0$ ), despite the usual label of “heavy-hole” band. We therefore refrain from referring to heavy or light holes in this work, adopting instead the terminology “first” (or “top”), and “second” bands. For  $m_z^*$ , the top band remains heaviest for all  $x$  considered here, and is a smooth function of the strain. These results are in reasonable agreement with several recent experiments [4–6], and they agree very well with Ref. [7], in which band nonparabolicity is explicitly accounted for. We note that although  $m_x^*$  appears to change abruptly in Fig. 3(a), smooth behavior is recovered when considering the narrower range of  $x=0$ –0.01.

Figure 4 shows the corresponding results for the energy dispersion of the valence-band edges. In the limit  $x \rightarrow 0$ , the top two bands become degenerate, and the split-off band is lower in energy by an amount  $\Delta = 0.29 \mu\text{eV}$ , which compares well with the experimentally measured value of  $0.296 \mu\text{eV}$  [17]. For  $x > 0$ , the band degeneracy is lifted by a significant amount, of order 100 meV for typical quantum-well heterostructures. In contrast with the effective mass, no abrupt change occurs for the valence-band edges near  $x=0$ .

To summarize the present results, DFT predicts a sudden change in the in-plane mass of the top band as the strain decreases from zero, with  $m_x$  becoming very light. Moreover, the degeneracy of the top two bands is lifted, and the energy splitting between all the bands is enhanced. These results are all consistent with recent experiments.

## B. $\mathbf{k}\cdot\mathbf{p}$ Analysis

$\mathbf{k}\cdot\mathbf{p}$  theory allows us to explore the mechanisms that cause the changes in the band structure and clarify their separate roles. In Fig. 5, we plot the edges of the top three valence bands, as a function of either strain or SOC. By following the progression from a single sixfold-degenerate band (center panel) to three twofold-degenerate bands (outer panels), we infer that the splitting of the top two bands requires both strain and SOC. The calculations also show that the hybridization of the topmost bands occurs at second order, via strain-induced coupling to the split-off band. Since this effect is weak, the total angular momentum in the top band, which defines the qubit, is still given by  $j=3/2$  and  $m_j=\pm 3/2$  to a good approximation, as indicated in the figure. Spin flips with  $\Delta m_s = \pm 1$  are allowed by EDSR, however, via the Rashba coupling mechanism described above.

In the  $\mathbf{k}\cdot\mathbf{p}$  calculations, we note that strain has been introduced perturbatively. Hence, although the energy splitting of the lowest valence band is exact when  $\varepsilon = 0$ , since it is taken as an input parameter, the calculated energies become increasingly inaccurate for higher strain values. For example, when  $\varepsilon = -1\%$ , the more accurate DFT result of  $\Delta=0.53 \mu\text{eV}$  is  $>50\%$  larger than the  $\mathbf{k}\cdot\mathbf{p}$  estimate. Likewise, the  $\mathbf{k}\cdot\mathbf{p}$  energy splitting of  $0.06 \mu\text{eV}$  between the top two valence bands is approximately half the DFT estimate of  $0.13 \mu\text{eV}$ .

To summarize, the  $\mathbf{k}\cdot\mathbf{p}$  theory reproduces the general features of the band structure that was obtained more

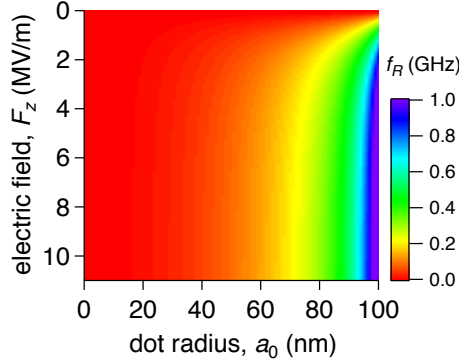


FIG. 6. Color map of the EDSR Rabi frequency  $f_R$  as a function of both the vertical electric field  $F_z$  and the effective dot radius  $a_0$ , with magnetic field  $B_z=0.06$  T, quantum well width  $d=20$  nm, and microwave driving amplitude [44]  $E_{ac}=0.1$  MV/m. All materials parameters assume a Si concentration of  $x=0.25$  in the barrier alloy.

rigorously using DFT. Although  $\mathbf{k}\cdot\mathbf{p}$  methods are less accurate than DFT, they allow us to clarify that both strain and SOC are required to fully lift the band degeneracy at  $\mathbf{k}=0$ .

### C. Quantum Well Corrections to the Energy

The energies plotted in Fig. 4 were obtained without including the quantum-well subband confinement energies, which differ for different bands, and can be sizeable. Here we show that the subband contribution to the hole energy does not compromise the energy splitting between the top two valence bands or change the effective ordering between them.

The subband energies differ for the top two valence bands due to their different effective masses. We can estimate these effects by assuming a triangular, vertical confinement potential, as in Eq. (6). Here, we assume an electric field value of  $F_z \approx ep/\epsilon$ , which is the field required to accumulate a 2D hole gas with density  $p = 4 \times 10^{11}$  cm $^{-2}$ , and we linearly interpolate the dielectric constant in the  $\text{Si}_x\text{Ge}_{1-x}$  barrier layer, obtaining the relation  $\epsilon(x) = (16.2 - 4.5x)\epsilon_0$ , where  $\epsilon_0$  is the vacuum permittivity. We further assume that the vertical extent of the wavefunction is less than the quantum well width, allowing us to ignore the bottom edge of the well. The triangular potential has known solutions [45], yielding a confinement energy of  $2.34 E_0$  for the first subband and  $4.09 E_0$  for the second subband, where  $E_0 = (\hbar^2 e^4 p^2 / 2m_z^* \epsilon^2)^{1/3}$  is a characteristic energy scale and  $m_z^*$  depends on both the alloy composition and the particular valence band. (Note that we do not consider band-nonparabolicity effects here, although they can be significant due to the large energies involved.) In this way, when  $x=0.25$ , we obtain a total energy splitting (including both band and subband energies) of 140 meV for the lowest-energy confined holes in the first and sec-

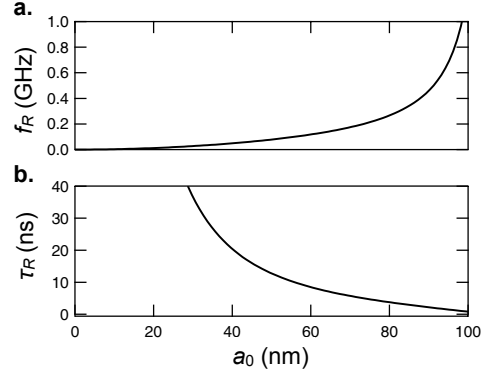


FIG. 7. Calculated values of (a) the EDSR Rabi frequency  $f_R$ , and (b) the corresponding  $X_{2\pi}$  gate time ( $\tau_R=1/f_R$ ), as a function of the effective dot radius  $a_0$ . Here, the simulation parameters are the same as in Fig. 6, with  $F_z = 4.5$  MV/m.

ond valence bands, with the first band still having the lowest energy. In comparison, the energy splitting between the first and second subbands within the top valence band, is 27.7 meV, which therefore represents the predominant leakage channel for the qubit. We conclude that band and subband excitations of the qubit level are much larger than other relevant energy scales in this system, including the thermal energy of the hole reservoirs (5-15  $\mu$ eV), the inter-dot tunnel couplings ( $\sim 200$   $\mu$ eV), and exchange interactions ( $\sim 200$   $\mu$ eV).

### D. Rabi Frequency Estimates

In Sec. II D, particularly in Eq. (14), we obtained general results for the EDSR Rabi frequency  $f_R$  as a function of system parameters. In Fig. 6, we now plot the dependence of the Rabi frequency on the dot radius  $a_0$  and the vertical electric field  $F_z$ . In Fig. 7, we further show a line-cut through this data, and a corresponding plot of  $\tau_R = 1/f_R$ , representing the gate time for an  $X_{2\pi}$  gate operation. Generally, we find that larger dots yield faster gate operations due to their smaller orbital energies. (We note that, for sufficiently large  $a_0$ , the perturbative methods used here become inaccurate.) To take an example, for a typical vertical field of 4.8 MV/m and effective dot radii in the range of 30-60 nm, Rabi frequencies can be of order 0.2 GHz, corresponding to a 5 ns gate time for an  $X_\pi$  gate. Such fast gates are very promising for high-fidelity quantum gate operations.

## IV. DISCUSSION AND CONCLUSIONS

Recent experimental work has already demonstrated that holes in germanium are promising as qubits. In this work, we have explored how confinement and strain are critical for achieving such strong performance, particularly in the context of EDSR-based gate operations. We

have also demonstrated that operating the qubits in an out-of-plane magnetic field may be advantageous because of the highly anisotropic  $g$ -factor.

To conclude, we comment on the expected decoherence mechanisms affecting Ge hole spins. As mentioned in the introduction, hyperfine interactions are suppressed for hole spins due to the  $p$ -orbital character of the valence band [2, 3], and the low natural abundance (<8%) of Ge isotopes with nonzero nuclear spin, which can be further reduced by isotopic purification [46]. However, charge noise is ubiquitous in semiconductor devices [47], including Ge quantum dots, particularly in the vicinity of the gate oxides. Although the poor quality of Ge oxides could exacerbate this problem, the simple inclusion of a Si capping layer should bring Ge/SiGe on par with related systems, such as Si-based qubits. Similarly, phonon noise should be similar in Ge and Si-based devices; in both cases, phonon effects are much weaker than in GaAs charge [48] or spin qubits [49, 50], due to the absence of piezoelectric phonons. Hence, hole spins in Ge quantum wells should be relatively well protected from their environment, making them particularly strong candidates for quantum dot qubits.

## ACKNOWLEDGEMENTS

We are grateful to D. J. Paul, G. Scappucci, D. E. Savage, O. P. Sushkov, D. S. Miserev and M. A. Eriksson for illuminating discussions and helpful information. Work in Brazil was performed as part of the INCT-IQ and supported by Centro Nacional de Processamento de Alto Desempenho em São Paulo (CENAPAD-SP, project UNICAMP/FINEP-MCT), CNPq (304869/2014-7, 308251/2017-2, and 309861/2015-2), and FAPERJ (E-26/202.915/2015 and 202.991/2017). Work in Australia was supported by the Australian Research Council Centre of Excellence in Future Low-Energy Electronics Technologies (project CE170100039). Work in the U.S.A. was supported in part by ARO (W911NF-17-1-0274 and W911NF-17-1-0257), NSF (OISE-1132804), and the Vannevar Bush Faculty Fellowship program sponsored by the Basic Research Office of the Assistant Secretary of Defense for Research and Engineering and funded by the Office of Naval Research through grant N00014-15-1-0029. The views and conclusions contained in this document are those of the authors and should not be interpreted as representing the official policies, either expressed or implied, of the Army Research Office (ARO), or the U.S. Government. The U.S. Government is authorized to reproduce and distribute reprints for Government purposes notwithstanding any copyright notation herein.

---

[1] M. Friesen, M. A. Eriksson, and S. N. Coppersmith, *Appl. Phys. Lett.* **89**, 202106 (2006).

[2] D. V. Bulaev and D. Loss, *Phys. Rev. Lett.* **98**, 097202 (2007).

[3] K. De Greve, P. L. McMahon, D. Press, T. D. Ladd, D. Bispinck, C. Schneider, M. Kamp, L. Worschech, S. Höfling, A. Forchel, and Y. Y., *Nature Phys.* **7**, 872 (2011).

[4] A. Dobbie, M. Myronov, R. J. H. Morris, A. H. A. Hassan, M. J. Prest, V. A. Shah, E. H. C. Parker, T. E. Whall, and D. R. Leadley, *Appl. Phys. Lett.* **101**, 172108 (2012).

[5] N. W. Hendrickx, D. P. Franke, A. Sammak, M. Kouwenhoven, D. Sabbagh, L. Yeoh, R. Li, M. L. V. Tagliaferri, M. Virgilio, G. Capellini, G. Scappucci, and M. Veldhorst, *Nature Commun.* **9**, 2835 (2018).

[6] C. Morrison and M. Myronov, *Phys. Status Solidi A* **213**, 2809 (2016).

[7] M. Lodari, A. Tosato, D. Sabbagh, M. A. Schubert, G. Capellini, A. Sammak, M. Veldhorst, and G. Scappucci, *Phys. Rev. B* **100**, 041304(R) (2019).

[8] S. Nadj-Perge, S. M. Frolov, E. P. A. M. Bakkers, and L. P. Kouwenhoven, *Nature* **468**, 1084 (2010).

[9] Y. Hu, F. Kuemmeth, C. M. Lieber, and C. M. Marcus, *Nature Nano.* **7**, 47 (2012).

[10] R. Li, F. E. Hudson, A. S. Dzurak, and A. R. Hamilton, *Nano. Lett.* **15**, 7314 (2015).

[11] S. D. Liles, R. Li, C. H. Yang, F. E. Hudson, M. Veldhorst, A. S. Dzurak, and A. R. Hamilton, *Nature Commun.* **9**, 3255 (2018).

[12] L. Vukušić, J. Kukučka, H. Watzinger, J. M. Milem, F. Schäffler, and G. Katsaros, *Nano. Lett.* **18**, 7141 (2018).

[13] H. Watzinger, J. Kukučka, L. Vukušić, F. Gao, T. Wang, F. Schäffler, J.-J. Zhang, and G. Katsaros, *Nature Commun.* **9**, 3902 (2018).

[14] W. J. Hardy, C. T. Harris, Y.-H. Su, Y. Chuang, J. Moussa, L. N. Maurer, J.-Y. Li, T.-M. Lu, and D. R. Luhman, *Nanotechn. **30***, 215202 (2019).

[15] N. W. Hendrickx, D. P. Franke, A. Sammak, G. Scappucci, and M. Veldhorst, *Nature* **577**, 487 (2020).

[16] A. Sammak, D. Sabbagh, N. W. Hendrickx, M. Lodari, B. Paquelet Wuetz, A. Tosato, L. Yeoh, M. Bollani, M. Virgilio, M. A. Schubert, P. Zaumseil, G. Capellini, M. Veldhorst, and G. Scappucci, *Advanced Functional Materials* **29**, 1807613 (2019).

[17] F. Schäffler, *Semicond. Sci. Techn.* **12**, 1515 (1997).

[18] S. J. Angus, A. J. Ferguson, A. S. Dzurak, and R. G. Clark, *Nano Lett.* **7**, 2051 (2007).

[19] K. Eng, T. D. Ladd, A. Smith, M. G. Borselli, A. A. Kislev, B. H. Fong, K. S. Holabird, T. M. Hazard, B. Huang, P. W. Deelman, I. Milosavljevic, R. Schmitz, R. S. Ross, M. F. Gyure, and A. T. Hunter, *Sci. Adv.* **1**, e1500214 (2015).

[20] D. M. Zajac, T. M. Hazard, X. Mi, K. Wang, and J. R. Petta, *Appl. Phys. Lett.* **106**, 223507 (2015).

[21] D. L. Harame, S. J. Koester, G. Freeman, P. Cottrel, K. Rim, G. Dehlinger, D. Ahlgren, J. S. Dunn, D. Greenberg, A. Joseph, F. Anderson, J.-S. Rieh, S. A. S. T. Onge, D. Coolbaugh, V. Ramachandran, J. D. Cressler,

and S. Subbanna, *Applied Surface Science* **224**, 9 (2004).

[22] D. J. Paul, *Laser Photon. Rev.* **4**, 610 (2010).

[23] Y.-H. Su, Y. Chuang, C.-Y. Liu, J.-Y. Li, and T.-M. Lu, *Phys. Rev. Materials* **1**, 044601 (2017).

[24] F. K. LeGoues, R. Rosenberg, T. Nguyen, F. Himpsel, and B. S. Meyerson, *J. Appl. Phys.* **65**, 1724 (1989).

[25] D. Laroche, S.-H. Huang, Y. Chuang, J.-Y. Li, C. W. Liu, and T. M. Lu, *Appl. Phys. Lett.* **108**, 233504 (2016).

[26] P. Blaha, K. Schwarz, G. Madsen, D. Kvasnicka, and J. Luitz, *WIEN2k: An Augmented Plane Wave plus Local Orbitals Program for Calculating Crystal Properties* (T. U. Vienna, Austria, Vienna, 2001).

[27] G. K. H. Madsen, P. Blaha, K. Schwarz, E. Sjöstedt, and L. Nordström, *Phys. Rev. B* **64**, 195134 (2001).

[28] O. K. Andersen, *Phys. Rev. B* **12**, 3060 (1975).

[29] E. Sjöstedt, L. Nordström, and D. J. Singh, *Solid State Commun.* **114**, 15 (2000).

[30] F. Tran and P. Blaha, *Phys. Rev. Lett.* **102**, 226401 (2009).

[31] A. D. Becke and E. R. Johnson, *J. Chem. Phys.* **124**, 221101 (2006).

[32] J. Wortman and R. Evans, *J. Appl. Phys.* **36**, 153 (1965).

[33] G. L. Bir and G. E. Pikus, *Symmetry and Strain Induced Effects in Semiconductors* (Wiley, New York, 1974).

[34] C. G. Van de Walle, *Phys. Rev. B* **39**, 1871 (1989).

[35] J. M. Luttinger, *Phys. Rev.* **102**, 1030 (1956).

[36] M. V. Fischetti and S. E. Laux, *J. Appl. Phys.* **80**, 2234 (1996).

[37] G. Bastard, E. E. Mendez, L. L. Chang, and L. Esaki, *Phys. Rev. B* **28**, 3241 (1983).

[38] E. Marcellina, A. R. Hamilton, R. Winkler, and D. Culcer, *Phys. Rev. B* **95**, 075305 (2017).

[39] Y. Tokura, W. G. van der Wiel, T. Obata, and S. Tarucha, *Phys. Rev. Lett.* **96**, 047202 (2006).

[40] R. Winkler, *Spin-Orbit Coupling Effects in Two-Dimensional Electron and Hole systems* (Springer, Berlin, 2003).

[41] V. Fock, *Zeitschrift für Physik* **47**, 446 (1928).

[42] C. G. Darwin, *Mathematical Proceedings of the Cambridge Philosophical Society* **27**, 86 (1931).

[43] E. Kawakami, P. Scarlino, D. R. Ward, F. R. Braakman, D. E. Savage, M. G. Lagally, M. Friesen, S. N. Coppersmith, M. A. Eriksson, and L. M. K. Vandersypen, *Nature Nano.* **9**, 666 (2014).

[44] J. Salfi, J. A. Mol, D. Culcer, and S. Rogge, *Phys. Rev. Lett.* **116**, 246801 (2016).

[45] J. H. Davies, *The Physics of Low-Dimensional Semiconductors* (Cambridge University Press, Cambridge, 1998).

[46] Y. Hu, H. O. H. Churchill, D. J. Reilly, J. Xiang, C. M. Lieber, and C. M. Marcus, *Nature Nano.* **2**, 622 (2007).

[47] O. E. Dial, M. D. Shulman, S. P. Harvey, H. Bluhm, V. Umansky, and A. Yacoby, *Phys. Rev. Lett.* **110**, 146804 (2013).

[48] T. Hayashi, T. Fujisawa, H.-D. Cheong, Y. H. Jeong, and Y. Hirayama, *Phys. Rev. Lett.* **91**, 226804 (2003).

[49] X. Hu, *Phys. Rev. B* **83**, 165322 (2011).

[50] J. K. Gamble, M. Friesen, S. N. Coppersmith, and X. Hu, *Phys. Rev. B* **86**, 035302 (2012).